Effect of electron–vibration interactions on the thermoelectric efficiency of molecular junctions

2012 Nanotechnology 23 275401

(http://iopscience.iop.org/0957-4484/23/27/275401)

Nanotechnology **23** (2012) 275401 (9pp) doi:10.1088/0957-4484/23/27/275401

Effect of electron–vibration interactions on the thermoelectric efficiency of molecular junctions

Bailey C Hsu, Chi-Wei Chiang and Yu-Chang Chen

Department of Electrophysics, National Chiao Tung University, 1001 University Road, Hsinchu 30010, Taiwan

E-mail: yuchangchen@mail.nctu.edu.tw

Received 10 January 2012, in final form 7 April 2012
Published 18 June 2012
Online at stacks.iop.org/Nano/23/275401

Abstract

From first-principles approaches, we investigate the thermoelectric efficiency of a molecular junction where a benzene molecule is connected directly to the platinum electrodes. We calculate the thermoelectric figure of merit ZT in the presence of electron–vibration interactions with and without local heating under two scenarios: linear response and finite bias regimes. In the linear response regime, ZT saturates around the electrode temperature $T_e = 25$ K in the elastic case, while in the inelastic case we observe a non-saturated and a much larger ZT beyond $T_e = 25$ K attributed to the tail of the Fermi–Dirac distribution. In the finite bias regime, the inelastic effects reveal the signatures of the molecular vibrations in the low-temperature regime. The normal modes exhibiting structures in the inelastic profile are characterized by large components of atomic vibrations along the current density direction on top of each individual atom. In all cases, the inclusion of local heating leads to a higher wire temperature T_w and thus magnifies further the influence of the electron–vibration interactions due to the increased number of local phonons.

(Some figures may appear in colour only in the online journal)

1. Introduction

The path to extreme device miniaturization has resulted in the rapid development of molecular electronics, where molecules are used as building blocks to form nanodevices [1, 2]. To ensure the functionality of such devices under finite biases, understanding the nonequilibrium electron quantum transport theory at the molecular level is crucial [3, 4]. The current-induced effects with nuclear degrees of freedom of molecule are important as they reveal information regarding the vibration of the molecule sandwiched between the electrodes. A number of current-induced effects, including those obtained by inelastic electron tunneling spectroscopy (IETS) and local heating, have been studied with an emphasis on the interplay between electrons and molecular vibrations [5–15].

Recent experiments have demonstrated energy conversion between thermal and electrical energy in single-molecule junctions [16–21]. The potential benefits of nanoscale engineering have generated interest in developing novel thermoelectric nanodevices such as nanorefrigerators, power generators, and self-powered atomic-scale transistors [22–25]. The thermoelectric efficiency of a single-molecule junction can be judged by the thermoelectric figure of merit ZT. In designing a low-temperature operated thermoelectric nanodevice, it is important to predict ZT from first-principles. It has been predicted that ZT increases as the length of a metallic atomic junction increases, while ZT decreases as the length of an insulating molecular junction increases [26].

Although considerable effort has been exerted to understand the inelastic effects on single-molecule junctions, only a few attempts have been made to study the inelastic effects on the thermoelectric properties of single-molecule junctions [27–33]. Previous studies have been primarily based on models or focused on a single vibrational mode coupling. In this work, we include all vibrational modes

in our calculations. In a recent study, Sergueev *et al* investigated the inelastic *ZT* in the linear response regime ($V_B \to 0$) within density functional theory, along with the nonequilibrium Green's function, and showed that the effect of electron–phonon interactions strongly depends on the junction configuration [34]. This approach improves over model calculations, which typically account for only a single mode, thereby missing the selection rule for important participant modes. Inelastic effects calculated from first-principles can provide complete information from all normal modes. In addition to the linear response regime, we also consider the thermoelectric efficiency in the finite bias regime. The Seebeck effect in the finite bias regime highlights the new possibility of engineering systems where a nonequilibrium current would enhance the thermopower [35, 36]. This finding is the motivation behind the investigation of the effects of electron–vibration interactions on the efficiency of thermoelectric effects in the finite bias ($V_B \neq 0$) regime. In this work, the Seebeck coefficients, the electron thermal conductance, and *ZT* are compared in the linear response and finite bias regimes with electron–vibration interactions, where all possible intrinsic vibrational modes of the junction are considered by excluding a few contact modes that strongly depend on the specific contact geometry between the molecule and the electrodes. The calculations show that the effect of electron–phonon interactions on the Seebeck coefficients is salient at high temperatures in the linear response regime because a significant fraction of electrons is thermally excited due to the tail of the Fermi–Dirac distribution. In the finite bias regime, we observe further the signatures of normal modes in the inelastic thermoelectric profiles at low temperatures.

The Seebeck coefficient is defined as $S = \mathrm{d}V/\mathrm{d}T$, where $\mathrm{d}V$ is the voltage difference caused by the temperature difference $\mathrm{d}T$ through the Seebeck effect [37]. The Seebeck coefficient is an intriguing transport quantity used to gauge thermoelectric efficiency, related not only to the magnitude but also to the slope of the density of states (DOS). As reported in [35], the Seebeck effect in a 4-Al atomic junction in the presence of electron–vibration scattering is enhanced at bias voltages corresponding to the longitudinal vibrational mode in the low-temperature regime, and further magnified through local heating. This demonstrates the advantage of a device based on molecular junctions because a larger Seebeck effect implies a better energy conversion capability. The thermoelectric figure of merit *ZT* depends on several physical factors: the Seebeck coefficient (S), the electrical conductance (σ), the electronic thermal conductance (κ_{el}), and the phononic thermal conductance (κ_{ph}). The thermoelectric efficiency can thus be generally described by the dimensionless thermoelectric figure of merit $ZT = S^2\sigma T/(\kappa_{el}+\kappa_{ph})$ where T is the average temperature in the source–drain electrodes [38].

Inspired by a recent experiment carried out by Kiguchi *et al* who measured a large conductance across a benzene molecular junction connected directly to platinum electrodes (Pt/benzene junction) [39], we explore the effects of electron–vibration interactions on the thermoelectric properties of a Pt/benzene junction. Due to the relatively small size of the Pt/benzene junction, our method which is suitable for coherent transport serves as an appropriate tool. The relaxed Pt/benzene junction configuration, as will be shown later, loses mirror symmetry. The highly tilted benzene molecule causes the streamline flow of the current to curve considerably to one side of the benzene ring, resulting in a nontrivial selection rule highly relevant to the details of the current density. Specifically, the investigation is performed through a comparison of the elastic and inelastic cases for the Seebeck coefficients, electron thermal conductance, and *ZT*, with and without local heating in the finite bias ($V_B = (\mu_R - \mu_L)/e \neq 0$) and linear response regimes ($V_B \to 0$) from first-principles.

2. Theoretical methods

The many-body Hamiltonian of the system under consideration is $H = H_{el}+H_{vib}+H_{el-vib}$ [5], where H_{el} is the electronic part of the Hamiltonian under the adiabatic approximation and H_{vib} is the ionic part of the Hamiltonian, which can be cast into a set of independent simple harmonic oscillators via a canonical transformation. H_{el-vib} is the part of the Hamiltonian for electron–vibration interactions which has the form of

$$H_{el-vib} = \sum_{\alpha,\beta,E_1,E_2,j}\left(\sum_{i,\mu}\sqrt{\frac{\hbar}{2M_i\omega_j}}A_{i\mu,j}J^{i\mu,\alpha\beta}_{E_1,E_2}\right) \times a^{\alpha\dagger}_{E_1}a^{\beta}_{E_2}(b_j + b^{\dagger}_j), \quad (1)$$

where $\alpha, \beta = \{L, R\}$, M_i is the mass of the ith atom, $A_{i\mu,j}$ is a canonical transformation between normal and Cartesian coordinates satisfying $\sum_{i,\mu}A_{i\mu,j}A_{i\mu,j'} = \delta_{j,j'}$, b_j is the annihilation operator corresponding to the jth normal mode ω_j, and $a^{L(R)}$ is the annihilation operator for electrons. The coupling constant $J^{i\mu,\alpha\beta}_{E_1,E_2}$ between electrons and the vibration of the ith atom in μ $(=x, y, z)$ component can be calculated as

$$J^{i\mu,\alpha\beta}_{E_1,E_2} = \int \mathrm{d}\mathbf{r}\int \mathrm{d}\mathbf{K}_{\parallel}[\Psi^{\alpha}_{E_1\mathbf{K}_{\parallel}}(\mathbf{r})]^*[\partial_{\mu}V^{ps}(\mathbf{r},\mathbf{R}_i)\Psi^{\beta}_{E_2\mathbf{K}_{\parallel}}(\mathbf{r})], \quad (2)$$

where $V^{ps}(\mathbf{r}, \mathbf{R}_i)$ is the pseudopotential representing the interaction between electrons and the ith ion, $\Psi^{\alpha(=L,R)}_{E\mathbf{K}_{\parallel}}(\mathbf{r})$ stands for the effective single-particle wavefunction of the entire system corresponding to incident electrons propagated from the left (right) electrode. These wavefunctions are calculated iteratively until convergence and self-consistency are achieved in the framework of DFT combined with the Lippmann–Schwinger equation [40]

$$\Psi^{\alpha}_{E\mathbf{K}_{\parallel}}(\mathbf{r}) = \Psi^{\alpha}_{0,E\mathbf{K}_{\parallel}}(\mathbf{r}) + \int \mathrm{d}\mathbf{r}_1\int \mathrm{d}\mathbf{r}_2 G(\mathbf{r},\mathbf{r}_1)V(\mathbf{r}_1,\mathbf{r}_2)\Psi^{\alpha}_{E\mathbf{K}_{\parallel}}(\mathbf{r}_2), \quad (3)$$

where G is the Green's function of the biased bimetallic electrodes with $V_B = (\mu_R - \mu_L)/e$, where $\mu_{R(L)}$ is the chemical potential deep in the right (left) electrode. We treat

the molecule as a scattering center. The potential $V(\mathbf{r}_1, \mathbf{r}_2)$ corresponds to the scattering potential represented by the following equation:

$$V(\mathbf{r}_1, \mathbf{r}_2) = V_{\rm ps}(\mathbf{r}_1, \mathbf{r}_2) + \Bigg\{ (V_{\rm xc}[n(\mathbf{r}_1)] - V_{\rm xc}[n_0(\mathbf{r}_1)]) + \int {\rm d}\mathbf{r}_3 \frac{\delta n(\mathbf{r}_3)}{|\mathbf{r}_1 - \mathbf{r}_3|} \Bigg\} \delta(\mathbf{r}_1 - \mathbf{r}_2), \quad (4)$$

where $V_{\rm ps}(\mathbf{r}_1, \mathbf{r}_2)$ is the electron–ion interaction potential [41], $V_{\rm xc}$ is the exchange–correlation potential in the local-density approximation, $n_0(\mathbf{r})$ is the electron density for the pair of biased bare electrodes, $n(\mathbf{r})$ is the electron density for the total system, and $\delta n(\mathbf{r})$ is their difference. To obtain a more accurate quantitative description of the electronic structures of molecular junctions, a more elaborate approximation of the exchange–correlation potential may be required [21]. $\Psi^{\alpha}_{0,E\mathbf{K}_\parallel}(\mathbf{r})$ is the wavefunction of the biased bimetallic junction before the inclusion of the molecule, which has the form $\Psi^{\alpha}_{0,E\mathbf{K}}(\mathbf{r}) = (2\pi)^{-1} {\rm e}^{{\rm i}\mathbf{K}\cdot\mathbf{R}} \cdot u^{\rm L(R)}_{E\mathbf{K}}(z)$, where $u^{\rm L(R)}_{E\mathbf{K}}(z)$ is the wavefunction of the bare electrodes along the z-direction before the inclusion of a nano-structured object. The wavefunction $u^{\rm L(R)}_{E\mathbf{K}}(z)$ is calculated by solving the coupled Shrödinger and Poisson equations iteratively until self-consistency is reached. Deep inside the electrodes ($z \to \pm\infty$), the right- and left-moving waves satisfy the scattering boundary conditions

$$u^{\rm L}_{E\mathbf{K}}(z) = \sqrt{\frac{m}{2\pi\hbar^2 k_{\rm L}}} \times \begin{cases} {\rm e}^{{\rm i}k_{\rm L}z} + R_{\rm L}{\rm e}^{-{\rm i}k_{\rm L}z} & z \to -\infty \\ T_{\rm L}{\rm e}^{{\rm i}k_{\rm R}z} & z \to \infty \end{cases}, \quad (5)$$

and

$$u^{\rm R}_{E\mathbf{K}}(z) = \sqrt{\frac{m}{2\pi\hbar^2 k_{\rm R}}} \times \begin{cases} T_{\rm R}{\rm e}^{-{\rm i}k_{\rm L}z} & z \to -\infty \\ {\rm e}^{-{\rm i}k_{\rm R}z} + R_{\rm R}{\rm e}^{{\rm i}k_{\rm R}z} & z \to \infty \end{cases}, \quad (6)$$

where $\mathbf{K}$ is the electron momentum in the plane parallel to the electrode surfaces, and z is the coordinate parallel to the direction of the current. Chemical potentials deep in the electrodes are maintained by the external bias. A basis of 3920 plane waves is chosen in the current calculations. Localized states are obtained by a direct diagonalization of the full Hamiltonian.

The electronic and phononic parts were first considered as the unperturbed Hamiltonian, and the electronic and nuclear degrees of freedom were assumed to be separable in the adiabatic approximation. The effects of electron–phonon interactions were considered using perturbation theory, thereby enabling the calculation of the inelastic thermal conductance. The right- and left-moving wavefunctions, weighted with the Fermi–Dirac distribution function according to their energies and temperatures, are applied to calculate the electric current and electron thermal current in the presence of the electron–vibration interactions through the respective equations

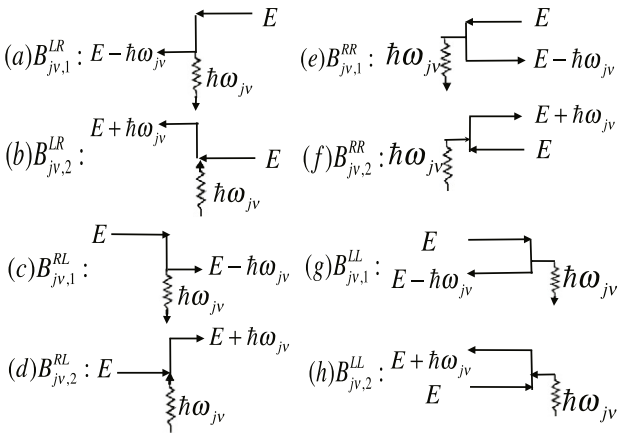

Figure 1. Feynman diagrams of the first-order electron–vibration scattering processes considered in this study.

$$I_{\rm el+vib}(\mu_{\rm L}, T_{\rm L}; \mu_{\rm R}, T_{\rm R}; T_{\rm w}) = \frac{2e}{h} \int {\rm d}E[(f^{\rm R}_E - f^{\rm L}_E) - (\tilde{B}^{\rm R} - \tilde{B}^{\rm L})]\tau(E), \quad (7)$$

and

$$J^{\rm L(R)}_{\rm el,el+vib}(\mu_{\rm L}, T_{\rm L}; \mu_{\rm R}, T_{\rm R}; T_{\rm w}) = \frac{2}{h} \int {\rm d}E[(f^{\rm R}_E - f^{\rm L}_E) - (\tilde{B}^{\rm R} - \tilde{B}^{\rm L})]\tau(E)(E - \mu_{\rm L(R)}), \quad (8)$$

where $f^{\rm L(R)}_E = 1/\{\exp[(E - \mu_{\rm L(R)})/(k_{\rm B}T_{\rm L(R)})] + 1\}$ is the Fermi–Dirac distribution function describing the statistics of electrons deep in the left (right) electrode with temperature $T_{\rm L(R)}$ and chemical potential $\mu_{\rm L(R)}$. The transmission function $\tau(E) = \frac{\pi\hbar^2}{m{\rm i}} \int {\rm d}\mathbf{r}_\parallel \int {\rm d}\mathbf{K}_\parallel (\Psi^{\rm R*}_{EK_\parallel} \nabla \Psi^{\rm R}_{EK_\parallel} - \nabla \Psi^{\rm R*}_{EK_\parallel} \Psi^{\rm R}_{EK_\parallel})$ is calculated from the electronic part of the wavefunctions $\Psi^{\rm R}_{EK_\parallel}$. The terms $\tilde{B}^{\rm L(R)}$ represent the corrections to the elastic current considering the eight first-order scattering processes depicted in figure 1 [35],

$$\tilde{B}^{\alpha} = \sum_j [\langle |B^{\beta,\alpha}_{j,k}|^2 \rangle f^{\alpha}_E (1 - f^{\beta}_{E\pm\hbar\omega_j}) - \langle |B^{\alpha\alpha}_{j,k}|^2 \rangle f^{\alpha}_E (1 - f^{\alpha}_{E\pm\hbar\omega_j})], \quad (9)$$

where $\alpha, \beta = \{{\rm L}, {\rm R}\}$ and $\alpha \neq \beta$. The $B^{\rm RR}_{j,1(2)}$ and $B^{\rm LR}_{j,1(2)}$ denoted in equation (9) are

$$B^{\alpha{\rm R}}_{j,1(2)} = {\rm i}\pi \sum_{i\mu} \sqrt{\frac{\hbar}{2M_i\omega_j}} A_{i\mu,j} J^{i\mu,\alpha R}_{E\pm\hbar\omega_j,E} D^{\alpha}_{E\pm\hbar\omega_j} \sqrt{\delta + \langle n_j \rangle}, \quad (10)$$

where $\alpha = \{{\rm L}, {\rm R}\}$, and $\delta = 0$ (1) represents the process of phonon emission (absorption). The other two terms in equation (9) can be obtained by the relations $B^{\rm LL}_{j,1(2)} = -B^{\rm RR}_{j,1(2)}$ and $B^{\rm RL}_{j,1(2)} = -B^{\rm LR}_{j,1(2)}$. Two major processes lead to the equilibrium local temperature in a nanojunction. One is due to the electron–vibration interaction that occurs in the atomic

region of the junction; the other is due to the dissipation of heat energy to the bulk electrodes via thermal transport. We assume that the energy generated in the atomic region via inelastic electron–vibration scattering and the energy dissipated to the electrodes via thermal current finally reach equilibrium such that a well-defined local temperature can be calculated and measured in the atomic region [10]. The reason for the single temperature for multiple vibrational modes is exactly the same as for that in the bulk system. When the bulk crystal reaches the equilibrium temperature T, the temperature T determines the distributions of the occupations of all phonon branches. In our system, the local temperature in the atomic region determines the number of phonons occupying each phonon mode. The statistical behavior of the multiple vibrational modes and their probabilities in the overall distributions are described by the Bose–Einstein distributions $\langle n_j\rangle = 1/\{\exp[\hbar\omega_j/(k_{\rm B}T_{\rm w})] - 1\}$, where $T_{\rm w}$ is the effective wire temperature due to local heating and $\langle n_j\rangle$ is the statistical average of the occupation number of the jth normal mode. This effective local temperature is informative regarding the stability and performance of electronic devices and is thus useful to both theorists and experimentalists. The local temperature $T_{\rm w}$ is obtained when the power generated in the central region via the electron–vibration interactions balances the rate of thermal energy dissipated to the electrodes calculated using the weak-link model [35]. Note that our inelastic current in equation (7) is similar to the expression in [34] where the correction due to electron–vibration couplings is included in the transmission function.

We calculate the inelastic Seebeck coefficient based on the inelastic current described in equation (7), which is a function of $T_{\rm L}$, $T_{\rm R}$, $T_{\rm w}$, and $V_{\rm B} = (\mu_{\rm R} - \mu_{\rm L})/e$. We consider an extra current induced by an infinitesimal temperature difference (ΔT) across the junction. This current is counterbalanced by an extra current driven by a voltage (ΔV), which is induced by ΔT via the Seebeck effect, i.e.,

$$I_{\rm el+vib}(\mu_{\rm L}, T_{\rm L}; \mu_{\rm R}, T_{\rm R}) = \left[I_{\rm el+vib}\left(\mu_{\rm L}, T_{\rm L} - \frac{\Delta T}{2}; \mu_{\rm R}, T_{\rm R} + \frac{\Delta T}{2}\right) + I_{\rm el+vib}\left(\mu_{\rm L} - \frac{e\Delta V}{2}, T_{\rm L}; \mu_{\rm R} + \frac{e\Delta V}{2}, T_{\rm R}\right)\right] \Big/ 2. \tag{11}$$

After expanding the above equation to the first order in ΔT and ΔV, we obtain the inelastic Seebeck coefficient (defined as $S_{\rm el+vib} = \Delta V/\Delta T$)

$$S_{\rm el+vib} = -\frac{1}{e}\frac{\int {\rm d}E(\frac{\partial \tilde{f}_E^{\rm R}}{\partial T_{\rm R}} + \frac{\partial \tilde{f}_E^{\rm L}}{\partial T_{\rm L}})\tau(E)}{\int {\rm d}E(\frac{\partial \tilde{f}_E^{\rm R}}{\partial E} + \frac{\partial \tilde{f}_E^{\rm L}}{\partial E})\tau(E)}, \tag{12}$$

where $\frac{\partial \tilde{f}_E^{\alpha}}{\partial E} = \frac{\partial f_E^{\alpha}}{\partial E} - \sum_{j\in{\rm vib};k=1,2}(C_{\mu,j,k}^{{\rm R}\alpha} + C_{\mu,j,k}^{{\rm L}\alpha})$, $\frac{\partial \tilde{f}_E^{\alpha}}{\partial T_{\rm R}} = \frac{\partial f_E^{\alpha}}{\partial T_{\rm R}} - \sum_{j\in{\rm vib};k=1,2}(C_{T,j,k}^{{\rm R}\alpha} + C_{T,j,k}^{{\rm L}\alpha})$, $\alpha = \{{\rm L}, {\rm R}\}$ and the terms $C_{\mu,j,1(2)}^{\alpha{\rm R}}$ and $C_{T,j,1(2)}^{\alpha{\rm R}}$ are due to the electron–vibration interactions

$$C_{\mu,j,1(2)}^{\alpha{\rm R}} = \left[f_E^{\rm R}\frac{\partial f_{E\pm\hbar\omega_{jv}}^{\alpha}}{\partial E} - (1 - f_{E\pm\hbar\omega_j}^{\alpha})\frac{\partial f_E^{\rm R}}{\partial E}\right]\langle|B_{j,1(2)}^{\rm RR}|^2\rangle, \tag{13}$$

$$C_{T,j,1(2)}^{\alpha{\rm R}} = \left[\frac{E \pm \hbar\omega_j - \mu_\alpha}{T_{\rm R}} f_E^{\rm R}\frac{\partial f_{E\pm\hbar\omega_j}^{\alpha}}{\partial E} - \frac{E - \mu_{\rm R}}{T_{\rm R}}(1 - f_{E\pm\hbar\omega_j}^{\alpha})\frac{\partial f_E^{\rm R}}{\partial E}\right]\langle|B_{j,1(2)}^{\alpha{\rm R}}|^2\rangle, \tag{14}$$

where $\alpha = \{{\rm L}, {\rm R}\}$ and $B_{j,1(2)}^{\alpha\beta}$ are given by equation (10). The other two terms in equation (12) can be calculated with the following relations: $\frac{\partial \tilde{f}_E^{\rm L}}{\partial T} = \frac{\partial \tilde{f}_E^{\rm R}}{\partial T}(L \rightleftharpoons R)$ and $\frac{\partial \tilde{f}_E^{\rm L}}{\partial E} = \frac{\partial \tilde{f}_E^{\rm R}}{\partial E}({\rm L} \rightleftharpoons {\rm R})$, where ${\rm L} \rightleftharpoons {\rm R}$ represents the interchange between R and L. We see that, in the absence of electron–phonon scattering, equation (12) recovers the elastic Seebeck coefficient described in [42].

As shown in equation (8), when a bias is applied to the junction, the inelastic electron thermal currents that flow from the right and into the left electrode are $J_{\rm el,el+vib}^{\rm R}$ and $J_{\rm el,el+vib}^{\rm L}$, respectively. At finite bias, note that there is no conservation of thermal current between two interfaces since the thermal current can be converted into electric current. Therefore, we define the inelastic electron thermal conductance in the junction by taking the average of the inelastic thermal conductance at two interfaces, $\kappa_{\rm el}^{\rm el+vib} = (\Delta J_{\rm el,el+vib}^{\rm R}/\Delta T + \Delta J_{\rm el,el+vib}^{\rm L}/\Delta T)/2$, where $\Delta J_{\rm el,el+vib}^{\rm R} = J_{\rm el}(\mu_{\rm L}, T_{\rm L}; \mu_{\rm R}, T_{\rm R} + \Delta T) + J_{\rm el}(\mu_{\rm L}, T_{\rm L}; \mu_{\rm R} + e\Delta V, T_{\rm R}) - 2J_{\rm el}(\mu_{\rm L}, T_{\rm L}; \mu_{\rm R}, T_{\rm R})$, $\Delta J_{\rm el,el+vib}^{\rm L} = J_{\rm el}(\mu_{\rm L}, T_{\rm L} + \Delta T; \mu_{\rm R}, T_{\rm R}) + J_{\rm el}(\mu_{\rm L} + e\Delta V, T_{\rm L}; \mu_{\rm R}, T_{\rm R}) - 2J_{\rm el}(\mu_{\rm L}, T_{\rm L}; \mu_{\rm R}, T_{\rm R})$, and ΔV is the voltage induced by ΔT via the Seebeck effect. The inelastic electron thermal conductance after expanding the Fermi–Dirac distribution function in equation (7) to the first order in ΔT and ΔV is given by

$$\kappa_{\rm el}^{\rm el+vib} = \sum_{\alpha,\beta=\{{\rm L},{\rm R}\}}\frac{1}{2h}\left[eS(K_1^{\alpha\beta} - \xi_1) + \frac{K_2^{\alpha\beta}}{T_\alpha} - \xi_2\right], \tag{15}$$

where $K_n^{\alpha\beta} = -\int {\rm d}E(E - \mu_\alpha)(E - \mu_\beta)^{n-1}\frac{\partial f_E^{\beta}}{\partial E}\tau(E)$, $\xi_1 = \sum_{\alpha=\{{\rm L},{\rm R}\}}\sum_{j\in{\rm vib};k=1,2}\int {\rm d}E(E - \mu_\alpha)(C_{\mu,j,k}^{{\rm R}\alpha} + C_{\mu,j,k}^{{\rm L}\alpha})\tau(E)$, $\xi_2 = \sum_{\alpha=\{{\rm L},{\rm R}\}}\sum_{j\in{\rm vib};k=1,2}\int {\rm d}E(E - \mu_\alpha)(C_{T,j,k}^{{\rm R}\alpha} + C_{T,j,k}^{{\rm L}\alpha})\tau(E)$, and $C_{\mu(T),j,k}^{{\rm L(R)}\alpha}$ are given in equations (13) and (14). Clearly, in the absence of electron–phonon scattering with $T_{\rm L} = T_{\rm R}$, equation (15) recovers the electron thermal conductance described in [26].

We estimate the phonon thermal conductance using the weak-link model [43]. The phonon Hamiltonian of the molecular junction is modeled by $H_{\rm ep} = H_{\rm L} + H_{\rm R} + \delta H$ where $H_{\rm L(R)} = \sum_n \omega_n^{\rm L(R)}(b_n^{\rm L(R)})^\dagger b_n^{\rm L(R)}$ is the Hamiltonian of the left (right) electrode, where $\omega_n^{\rm L(R)}$ and $b_n^{\rm L(R)}$ are the phonon spectrum and phonon annihilation operator in the left and right electrodes, respectively. The molecule sandwiched between the electrodes is modeled by a harmonic spring with stiffness K described by $\delta H = \frac{1}{2}K(u_{\rm L}^z - u_{\rm R}^z)^2$, where $u_{\rm L(R)}^z$ is the normal component of the displacement field $\mathbf{u}(\mathbf{r})$ at the surface of the left (right) electrode [43]. The phonon thermal conductance,

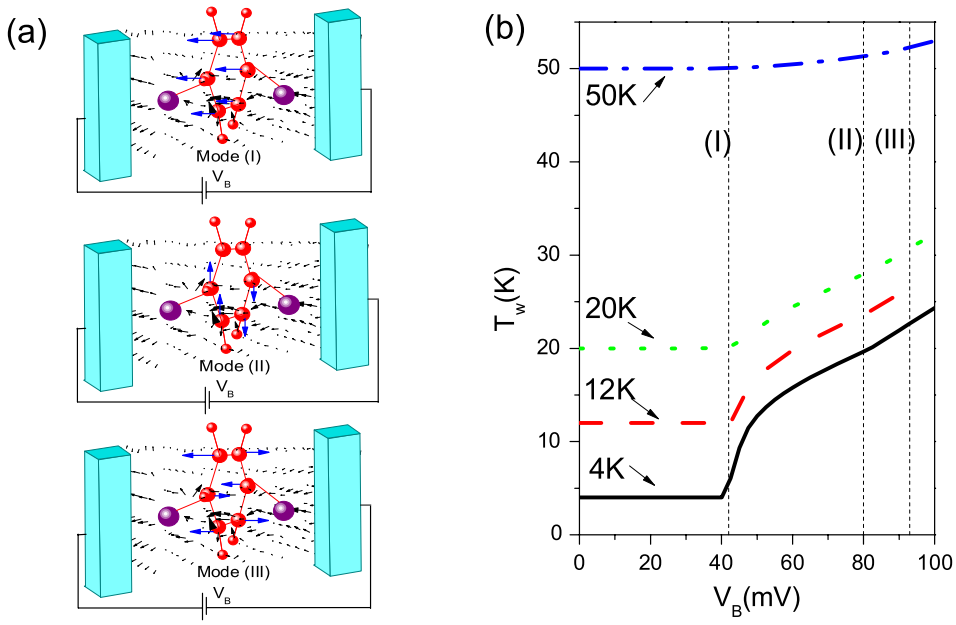

Figure 2. (a) Schematics of the three most important normal modes (modes (I)–(III) with energies of 42, 80, and 93 meV, respectively) in the inelastic profiles. The big (small) red balls represent carbon (hydrogen) atoms, and the purple balls represent Pt atoms. The blue arrow lines describe the vibrational pattern of the molecule. The black arrow lines represent the 3D current density vector plot at $V_B = 0.1$ V. The graph is plotted in log scale to aid visualization of the smaller current density. (b) The local wire temperature T_w versus V_B with the electrode temperature T_e set as 4, 12, 20, and 50 K. The vertical dotted lines refer to the biases corresponding to modes (I)–(III).

approximated by the weak-link model, can be obtained by $\kappa_{ph} = \frac{\pi K^2 C^2}{\hbar} \int_0^\infty dE\, E^3 \sum_{i=L,R} \frac{dn_i(E)}{dT_i}$, where the left (right) electrode is modeled as a phonon reservoir described by the Bose–Einstein distribution function $n_{L(R)}$; $N_{L(R)}(E) \approx CE$, where C is a constant, refers to the spectral density of surface phonon states at the left (right) electrode. The stiffness in the Pt/benzene junction has been estimated to be $K = 6.673\,02 \times 10^{-4}$ eV/a_0^2 by total energy calculations.

The thermoelectric figure of merit ZT depends on several physical factors: the Seebeck coefficient (S), the electrical conductance (σ), the electronic thermal conductance (κ_{el}), and the phononic thermal conductance (κ_{ph}). We calculate the inelastic ZT by $ZT = S_{el+vib}^2 \sigma_{el+vib} T/(\kappa_{el}^{el+vib} + \kappa_{ph})$ where T is the average temperature in the source–drain electrodes. The inelastic electrical conductance σ_{el+vib} is obtained by differentiating the inelastic current given by equation (7) with respect to the bias V_B, S_{el+vib} is obtained using equation (12), κ_{el}^{el+vib} is obtained using equation (15), and κ_{ph} is obtained using the weak-link model.

3. Results and discussion

The vibration frequencies represented by ω_j in the jth mode and the canonical transformation $A_{i\mu,j}$ are obtained in the Pt/benzene single-molecule junction using the Gaussian03 quantum chemistry code. We display the relaxed geometry in figure 2(a). The junction length is set to 9.6 au, and the closest distance between the benzene molecule and the electrodes is 4.1 au (left) and 4.1 au (right), respectively. The angle of the tilted benzene ring with respect to the z-axis is 37.9°. The inelastic effects are calculated from perturbation theory considering the scattering processes described in figure 1. It should be noted that the outermost layer of the platinum has to be included in the vibrational analysis to obtain an IETS with a mode identification in good agreement with the experimental data [39], where the first notable structure occurs at 42 mV corresponding to the longitudinal vibration of the molecule. To further justify the junction geometry, we also perform an isotope substitution of the carbon atoms and again obtain an IETS consistent with the experimental data, where the first important mode is shifted to 40 mV. The calculated conductance for the Pt/benzene system was high at approximately 0.58 G_0 in the linear response regime. The system, therefore, belongs to the strong coupling system ($G > 0.5$ G_0), and the conductance may be expected to show step-down features at bias voltages corresponding to the frequencies of the normal modes, implying that the effective transmission function with the electron–vibration interactions also shows the step-down features. These features agree well with the results of our current calculations.

As noted in equation (2), the coupling constants $J_{E_1,E_2}^{i\mu,\alpha\beta}$ ($\mu = x, y$, and z) are calculated from the current-carrying wavefunctions by first-principles. Thus, the coupling constants along the x-, y-, and z-directions are positively correlated with the current densities along the corresponding directions. Along with the canonical transformation matrix $A_{i\mu,j}$ (equation (1)), which provides information on the direction of the normal mode vibrations of the molecule, the mode selection rule is determined by the factor $|\Sigma_{i\mu} A_{i\mu,j} J_{E_1,E_2}^{i\mu,\alpha\beta}|$. The strength of the impact of electron–vibration interactions on the inelastic effects is positively correlated with this factor. Figure 3 shows the factors $|\Sigma_{i\mu} A_{i\mu,j} J_{E_1,E_2}^{i\mu,\alpha\beta}|$ for $\alpha = \beta =$ R with the energies E_1 and E_2 around the chemical

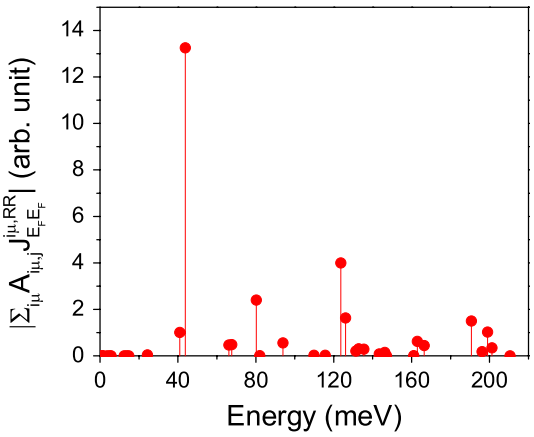

Figure 3. The factor $|\Sigma_{i\mu} A_{i\mu,j} J^{i\mu,RR}_{E_F,E_F}|$ for the normal modes with energies smaller than 200 meV.

potential for the normal modes with energies smaller than 200 meV. The magnitudes of these factors indicate that the contributions of normal modes to the inelastic effects significantly vary from mode to mode. To understand the rule of mode selection, we explore how the detailed current density flows through the nanojunction. We observe that the mode selection rule can be visualized by the current density and the normal mode vibrations. The important modes in the inelastic thermoelectric profile in the finite bias regime, where the modes are characterized by large components of atomic vibrations along the direction of the current density on atoms, are identified as discussed below.

Figure 2(a) shows that the current takes on a non-linear path and there is an uneven distribution of the current going through the top part of the benzene ring compared with the bottom part of the ring. More notably, the current tends to go around the carbon ring. We schematically show the three most significant normal modes (modes (I)–(III)) out of 42 possible modes in the inelastic profiles for $V_B <$ 100 mV. Mode (I), with an energy of 42 meV, has been experimentally observed in IETS [39]. This mode corresponds to a vibration of the benzene molecule as a whole, with a large component of motion along the z-direction (direction of the current). Mode (II), with an energy of 80 meV, shows that the left-side of the carbon ring vibrates downwards while the right-side vibrates upwards with a motion that is perpendicular to the z-direction. This mode has also been observed in the experimental IETS [39]. Mode (III), with an energy of 93 meV, shows that only the second-nearest neighbor vibrates in the same direction.

Figure 2(b) shows the effective local temperature T_w in the central region of the junction as a function of the bias for four different electrode temperatures $T_e = 4$, 12, 20, and 50 K. The local temperature is reached when the rate of heat generated in the molecule due to the current balances the rate of energy dissipated to the electrodes. The rate of heat generated in the molecule due to the current via the electron–vibration interactions is calculated from the Fermi golden rule. The rate of heat generated in the molecule is relatively insensitive to the temperature of the electrodes if tunneling is the primary conduction mechanism. An immediate sharp increase in the local temperature is observed around $V_B = 42$ mV, with which electrons gain enough energy eV_B to excite mode (I). The higher the electrode temperature is, the less prominent the temperature rise beyond 42 mV is. We take $T_e = 50$ K as an example where the signature of molecular vibrations is washed out. This finding may have resulted from the more efficient heat dissipation to electrodes because of a larger population of high energetic states facilitated by the higher electrode temperature, while the rate of heat generated in the central region was relatively unchanged. We also observe signals of vibrations of the molecule connected to contacts at the local temperature at biases of around 80 mV and 96 mV due to modes (II) and (III), respectively. For mode (II), where the motion of atoms is mostly transverse to the z-direction, the contribution to inelastic effects is still pronounced. This result is different from the case of the 4-Al linear atomic chain, where the observable jump in the profile of effective local temperatures appears *only* at biases corresponding to modes with motion along the z-direction. To illustrate the significance of mode (II), we draw a detailed comparison between the motion of normal modes and the current density. We observe that mode (II) has significant components of atom vibrations along the curved current-streamline flows around the tiled benzene molecule, as shown in figure 2(a). By careful inspection of all modes, we conclude that significant modes in the inelastic profiles require substantial components of atomic vibrations along the current-streamline flows of the top of each individual atom.

Figure 4(a) displays the Seebeck coefficients in the finite bias regime in three cases: 'elastic' (absence of electron–vibration interactions), 'inelastic' (in the presence of electron–vibration interactions and $T_w = T_e$), and 'inelastic + local heating' at different electrode temperatures. Inelastic + local heating means that the local wire temperature is included. The Seebeck coefficients at finite biases can reveal the signatures of vibrations of the molecule connected to the electrodes. The Pt/benzene system reveals n-type ($S < 0$) thermoelectric performance, implying that the slope of the transmission function is negative. The step-down feature of the effective transmission function attributable to the electron–vibration interactions results in the step-down feature of the inelastic Seebeck coefficients, as shown in figure 4(a). The first jump in the inelastic Seebeck coefficients occurs at 42 mV, corresponding to mode (I). Mode (I) is the most important mode, with the direction of the current density mostly in line with the vibrations of the atoms. In the low-temperature regime, electrons begin to excite the vibrations of the molecule as the bias exceeds the energy of mode (I). These effects increase the inelastic transmission functions resulting from the electron–vibration interactions, thus enhancing the magnitudes of the Seebeck coefficients around the biases, with eV_B being equal to the energies of mode (I). The jump increases with increasing electrode temperature because of the presence of a greater number of high-energy electrons that are capable of participating in the electron–vibration interactions resulting from the tail

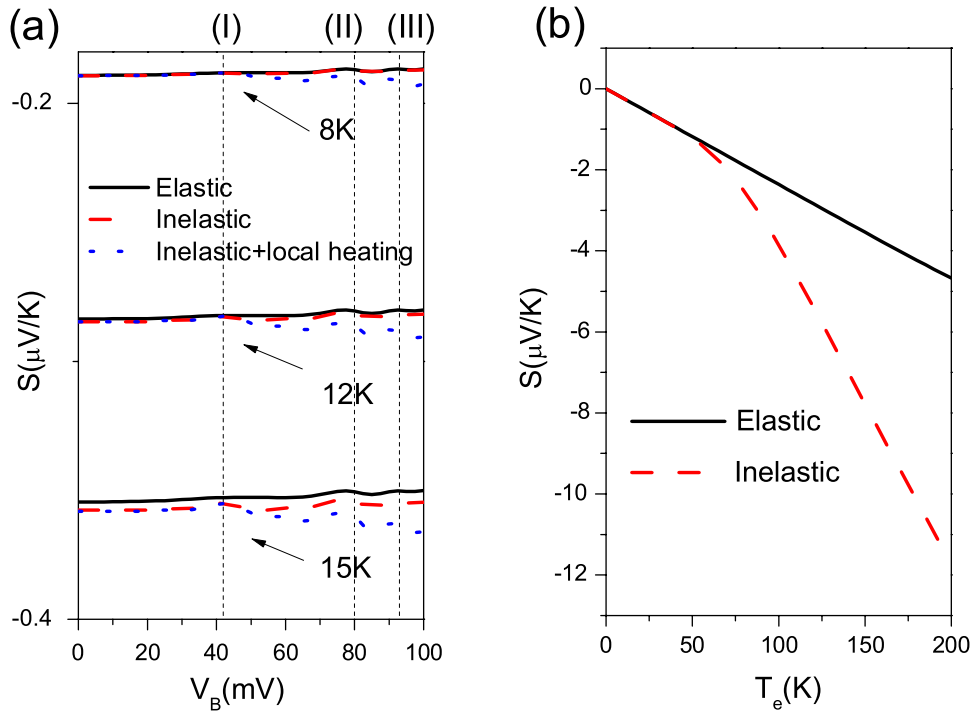

Figure 4. (a) Seebeck coefficients as a function of the applied bias in three cases: elastic (black solid line), inelastic without local heating (red dashed line), and inelastic with local heating (blue dotted line) for three different electrode temperatures $T_e = 8$, 12, and 15 K. (b) Seebeck coefficients with and without electron–vibration interactions as a function of the electrode temperature at zero applied bias.

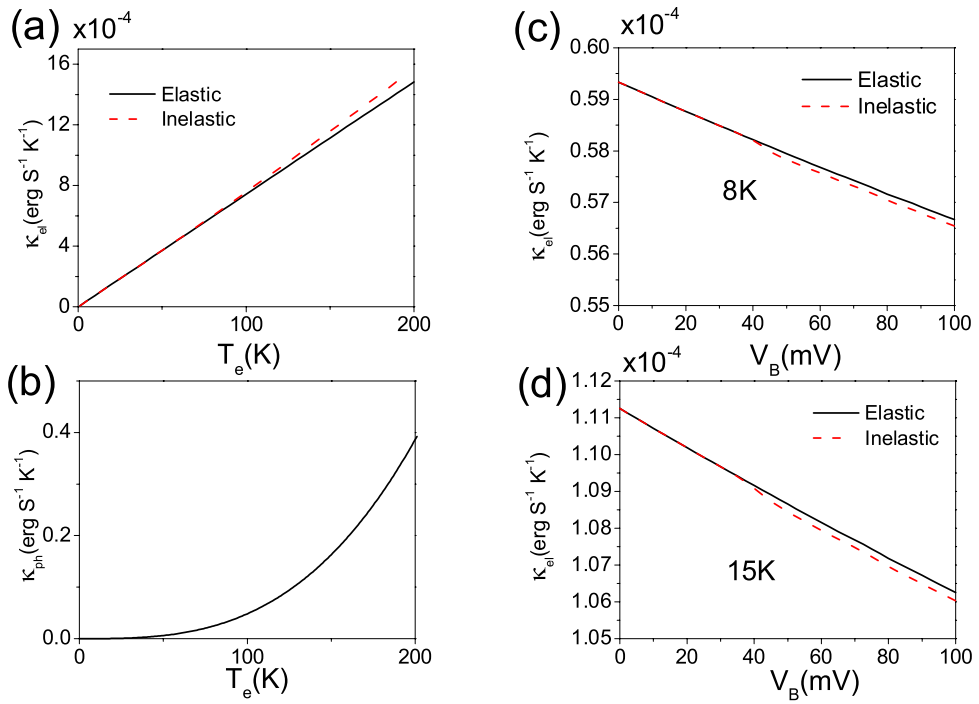

Figure 5. (a) Electron thermal conductance versus electrode temperature at zero applied bias. (b) Phonon thermal conductance versus electrode temperature. (c), (d) Electron thermal conductance as a function of the bias at (c) 8 K and (d) 15 K.

of the Fermi–Dirac distribution. The inclusion of local heating also enhances the inelastic Seebeck effect further because of the enhanced electron–vibration interactions of the increased population of local phonons attributable to the higher local temperature in the central region. The second drop in the inelastic Seebeck coefficients occurs at around $V_B = 80$ mV, corresponding to mode (II). As mentioned above, mode (II) becomes important in the inelastic Seebeck profiles because the curved current-streamline flows in line with the transverse vibrations. The differences between

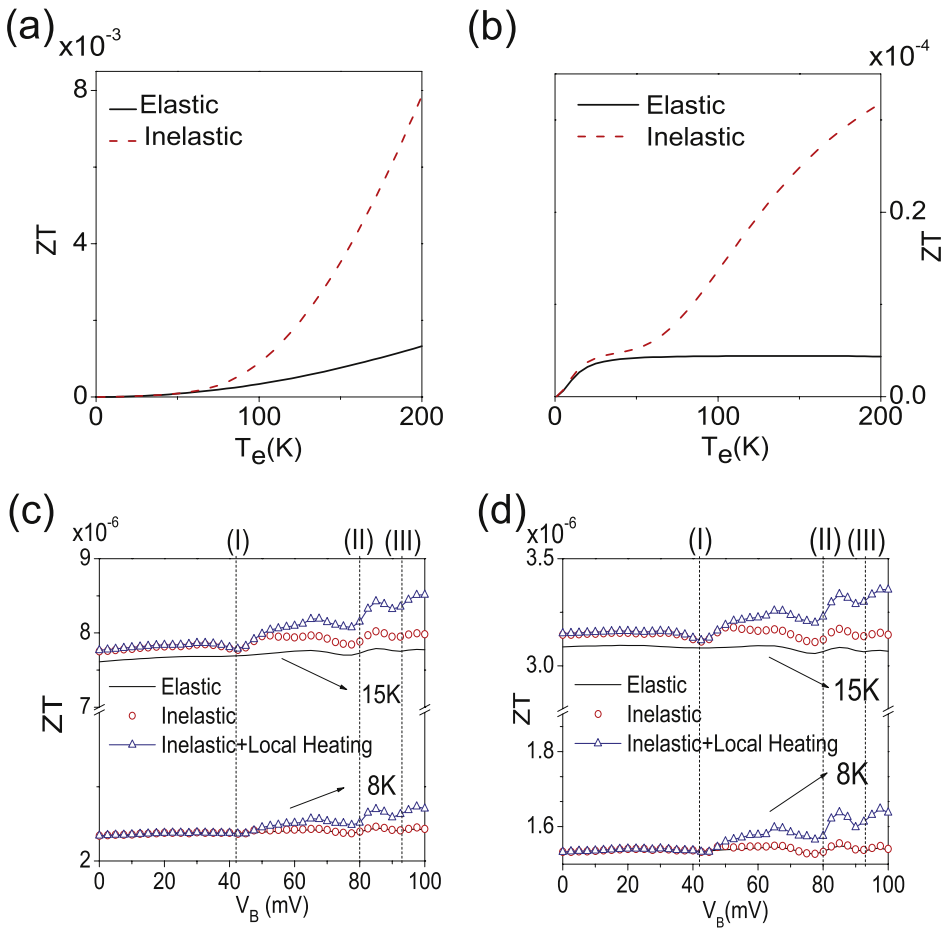

Figure 6. Thermoelectric figure of merit ZT (a) without κ_{ph} and (b) with κ_{ph} as a function of the temperature at zero bias for the elastic (black solid line) and inelastic (red dashed line) cases. Thermoelectric figure of merit ZT as a function of the source–drain bias V_B at $T_e = 8$ and 15 K (c) without κ_{ph} and (d) with κ_{ph}.

inelastic Seebeck coefficients with and without local heating are invisible in the high-temperature regime. Figure 4(b) compares the elastic and inelastic Seebeck coefficients in the linear response regime. We observe that the increased electrode temperature leads to larger Seebeck coefficients. The magnitude of inelastic Seebeck coefficients increases more rapidly beyond 50 K than the elastic one. This makes sense because more electrons are thermally excited at higher temperatures due to the tail of the Fermi–Dirac distribution. Consequently, more electrons possess enough energy to enhance the inelastic effects on the Seebeck coefficients.

Figure 5(a) presents comparisons between the elastic and inelastic electron thermal conductances as a function of temperature in the linear response regime. The onset of the larger inelastic electron thermal conductance appears around $T_e = 100$ K due to the tail of the Fermi–Dirac distribution. Figure 5(b) shows the phonon thermal conductance κ_{ph} as a function of the electrode temperature T_e. In the finite bias regime, the comparison of the elastic and inelastic electron thermal conductances again reveals the signature of molecular vibrations, which displays a drop in the electron thermal conductance at around $V_B = 42$ mV for $T_e = 8$ and 15 K, respectively, as shown in figures 5(c) and (d). In contrast to the Seebeck coefficients and electron thermal conductance which both show strong dependence on the temperature, the electrical conductance is insensitive to the temperature when tunneling is the major transport mechanism.

Based on the foregoing discussion, we now arrive at the elastic and inelastic thermoelectric efficiency ZT in the linear response and finite bias regimes. In the linear response regime, we present elastic and inelastic ZT values with and without κ_{ph} in figures 6(a) and (b), respectively. The comparison of inelastic and elastic ZT values without κ_{ph} in figure 6(a) shows that the electron–vibration interactions lead to a larger ZT when $T_e > 50$ K. Figure 6(b) shows that the inclusion of the phonon thermal conductance leads to an overall reduction of ZT in both the inelastic and the elastic cases. ZT saturates around $T_e = 25$ K in the elastic case. This result is in agreement with [26] that ZT saturates when T is larger than a characteristic temperature, defined as the temperature at which the electron thermal current equals the phonon thermal current. In the inelastic case, we no longer observe a saturated ZT value [26]. The thermoelectric figure of merit ZT continues to grow beyond $T_e = 50$ K attributed to the tail of the Fermi–Dirac distribution. In the finite bias regime, we compare ZT values as a function of the source–drain bias in three cases: ‘elastic’, ‘inelastic’, and ‘inelastic + local heating’

for different electrode temperatures, without (figure 6(c)) and with (figure 6(d)) κ_{ph}. Figures 6(c) and (d) show that in the finite bias regime, *ZT* can still be enhanced by the electron–vibration interactions. Moreover, *ZT* also reveals the signature of vibrations: *ZT* values start to increase at $V_B = 42$ mV corresponding to mode (I). We also observe that local heating further increases *ZT*. When κ_{ph} is included, the *ZT* value is suppressed substantially as shown in figure 6(d).

4. Conclusion

In conclusion, we have investigated the impact of electron–vibration interactions on thermoelectric efficiency in the linear response regime and the finite bias regime in the Pt/benzene junction, specifically via comparison among cases of elastic and inelastic, with and without local heating, for the Seebeck coefficients, the electronic thermal conductance, and *ZT*. This extends the case in which only a single vibrational mode or only the zero bias is considered. In contrast to the electrical conductance which is insensitive to the temperature, the Seebeck coefficients, the electron thermal conductance, and *ZT* all strongly depend on the temperature. In the linear response regime, the *ZT* value saturates around $T_e = 25$ K in the elastic case, whereas *ZT* no longer saturates in the inelastic case. The inelastic *ZT* increases beyond $T_e = 25$ K as the temperature increases. In the finite bias regime, these inelastic effects reveal the signature of the molecular vibrations in the low-temperature regime. We have identified normal modes that lead to significant structures in the inelastic profile. These modes are characterized by large components of atomic vibrations along the current density direction on top of each individual atom. In all cases, the inclusion of local heating leads to a higher wire temperature T_w and thus magnifies the influence of the electron–vibration interactions due to the increased number of local phonons. Based on these findings, we conclude that the electron–vibration interactions are advantageous to the thermoelectric efficiency in the Pt/benzene molecular junction.

Acknowledgments

The authors thank the National Science Council (Taiwan) for its support under Grant NSC 100-2112-M-009-012-MY3, the Ministry of Education, Aiming for Top University Plan (MOE ATU2), and the National Center for Theoretical Sciences. The authors also thank the National Center for High-performance Computing for computing time and facilities.

References

[1] Di Ventra M 2008 *Electrical Transport in Nanoscale Systems* (Cambridge: Cambridge University Press)
[2] Tao N J 2006 *Nature Nanotechnol.* **1** 173
[3] Nitzan A and Ratner M A 2003 *Science* **300** 1384
[4] Galperin M, Ratner M A and Nitzan A 2007 *J. Phys.: Condens. Matter* **19** 103201
[5] Chen Y C, Zwolak M and Di Ventra M 2003 *Nano Lett.* **3** 1691
[6] Chen Y C, Zwolak M and Di Ventra M 2004 *Nano Lett.* **4** 1709
[7] Chen Y C, Zwolak M and Di Ventra M 2005 *Nano Lett.* **5** 621
[8] Chen Y C 2008 *Phys. Rev.* B **78** 233310
[9] Kristensen I S, Paulsson M, Thygesen K S and Jacobsen K W 2009 *Phys. Rev.* B **79** 235411
[10] Huang Z, Xu B, Chen Y C, Di Ventra M and Tao N J 2006 *Nano Lett.* **6** 1240
[11] Yu L H, Zangmeister C D and Kushmerick J G 2007 *Phys. Rev. Lett.* **98** 206803
[12] Gagliardi A, Solomon G C, Pecchia A, Frauenheim T, Di Carlo A, Hush N S and Reimers J R 2007 *Phys. Rev.* B **75** 174306
[13] Troisi A and Ratner M A 2006 *Nano Lett.* **6** 1784
[14] Sergueev N, Roubtsov D and Guo H 2005 *Phys. Rev. Lett.* **95** 146803
[15] Paulsson M, Frederiksen T, Ueba H, Lorente N and Brandbyge M 2008 *Phys. Rev. Lett.* **100** 226604
[16] Ludoph B and van Ruitenbeek J M 1999 *Phys. Rev.* B **59** 12290
[17] Reddy P, Jang S Y, Segalman R A and Majumdar A 2007 *Science* **315** 1568
[18] Baheti K, Malen J A, Doak P, Reddy P, Jang S Y, Tilley T D, Majumdar A and Segalman R A 2008 *Nano Lett.* **8** 715
[19] Malen J A, Doak P, Baheti K, Tilley T D, Segalman R A and Majumdar A 2009 *Nano Lett.* **9** 1164
[20] Malen J A, Yee S K, Majumdar A and Segalman R A 2010 *Chem. Phys. Lett.* **491** 109
[21] Quek S Y, Choi H J, Louie S G and Neato J B 2011 *ACS Nano* **5** 551
[22] Liu Y S and Chen Y C 2011 *Appl. Phys. Lett.* **98** 213103
[23] Liu Y S, Hsu B C and Chen Y C 2011 *J. Phys. Chem.* C **115** 6111
[24] Liu Y S, Yao H T and Chen Y C 2011 *J. Phys. Chem.* C **115** 14988
[25] Bergfield J P, Solis M A and Stafford C A 2010 *ACS Nano* **4** 5314
[26] Liu Y S, Chen Y R and Chen Y C 2009 *ACS Nano* **3** 3497
[27] Entin-Wohlman O, Imry Y and Aharony A 2010 *Phys. Rev.* B **82** 115314
[28] Yang N, Zhang G and Li B arXiv:1106.5208v1 [cond-mat.mes-hall]
[29] Kuo D M T 2010 *Japan. J. Appl. Phys.* **49** 095205
[30] Leijnse M, Wegewijs M R and Flensberg K 2010 *Phys. Rev.* B **82** 045412
[31] Galperin M, Nitzan A and Ratner M A 2008 *Mol. Phys.* **106** 397
[32] Segal D 2005 *Phys. Rev.* B **72** 165426
[33] Ren J, Zhu J-X, Gubernatis J E, Wang C and Li B 2011 arXiv:1106.5208v1 [cond-mat.mes-hall]
[34] Sergueev N, Shin S, Kaviany M and Dunietz B 2011 *Phys. Rev.* B **83** 195415
[35] Hsu B C, Liu Y S, Lin S H and Chen Y C 2011 *Phys. Rev.* B **83** 041404(R)
[36] Esposito M, Lindenberg K and Van den Broeck C 2009 *Phys. Rev. Lett.* **102** 130602
[37] Dubi Y and Di Ventra M 2011 *Rev. Mod. Phys.* **83** 131
[38] Markussen T, Jauho A P and Brandbyge M 2009 *Phys. Rev.* B **79** 035415
[39] Kiguchi M, Tal O, Wohlthat S, Pauly F, Krieger M, Djukic D, Cuevas J C and van Ruitenbeek J M 2008 *Phys. Rev. Lett.* **101** 046801
[40] Lang N D 1995 *Phys. Rev.* B **52** 5335
[41] Bachelet G B, Hamann D R and Schlüter M 1982 *Phys. Rev.* B **26** 4199
[42] Liu Y S and Chen Y C 2009 *Phys. Rev.* B **79** 193101
[43] Patton K R and Geller M R 2001 *Phys. Rev.* B **64** 155320